



TECHNICAL ARTICLE

Influence of Initial Microstructure on the Hot Deformation Behavior of AZ80 Magnesium Alloy

Paresh Prakash, Jared Uramowski, Mary A. Wells, and Bruce W. Williams

Submitted: 8 January 2022 / Revised: 23 May 2022 / Accepted: 13 June 2022 / Published online: 27 July 2022

This research studies the hot deformation behavior of cast and extruded AZ80 magnesium alloys for forging applications. Uniaxial hot compression tests were carried out at a temperature of 400 °C and strain rates ranging from 0.001 to 0.1 s⁻¹, to various strain levels up to a true strain of 1. Detailed microstructure and texture characterizations of the deformed samples were performed using electron backscatter diffraction and x-ray diffraction techniques. The results show that multiple dynamic recrystallization (DRX) mechanisms were simultaneously active in both starting materials at all the tested deformation conditions, resulting in significant grain refinement. Cast and extruded samples showed the development of a similar microstructure, texture, and flow stress by a strain of 1, despite having very different starting microstructures. This was investigated by considering differences in DRX mechanisms and kinetics, and relative deformation mode activities. Since industrial forgings typically involve strains much higher than 1, comparable final microstructure and texture are expected in industrial-scale forgings of AZ80 at 400 °C, irrespective of the starting material state.

Keywords cast versus wrought AZ80, continuous dynamic recrystallization (CDRX), discontinuous dynamic recrystallization (DDRX), electron backscatter diffraction (EBSD), forging, microstructure, texture

1. Introduction

Magnesium-based alloys are becoming increasingly popular within the automotive industry owing to their significant weight saving potential compared to other metallic materials. Among the commercial grades of magnesium-based alloys currently available, high Al content AZ alloys (which have Al in the range of 6-9 wt.%) are the most popular for automotive applications, as they offer a good combination of castability and forgeability, are relatively less expensive, and are amenable to heat treatment. AZ91 alloy is by far the most used magnesium alloy in the automotive industry and is mainly used as a die cast alloy.

For fatigue critical applications such as in automotive suspension components, forging is the preferred fabrication route since it results in superior mechanical performance of the final component (Ref 1, 2). Magnesium-based alloys are

typically hot forged (usually at temperatures higher than about 200 °C (Ref 3)) since higher temperature activates the non-basal slip systems and dynamic recrystallization (DRX), both of which enhance the workability of the material (Ref 4-7). DRX in AZ alloys can take place through various mechanisms including grain boundary bulging induced discontinuous dynamic recrystallization (DDRX), grain fragmentation and recovery based continuous dynamic recrystallization (CDRX), twin dynamic recrystallization (TDRX), and particle stimulated nucleation (PSN) mechanisms (Ref 5, 8, 9). The material typically shows different dominant DRX mechanisms under different deformation conditions (Ref 10), although it is also possible for multiple DRX mechanisms to be active in the material simultaneously (Ref 11).

The starting material for forging can include both cast and wrought forms of the alloy. Cast material is less expensive and can be cast in a desired pre-form shape, easing the amount of forging needed to reach the final component shape. However, it is uncertain whether the strain induced during forging is sufficient to produce a homogeneous fine-grained microstructure from the cast material, which is beneficial for enhanced mechanical performance of the final component. Such strain levels, if known, can be used to compute the preform shape which would require the minimum amount of forging to reach the final component geometry, while still having the required strain throughout the component to permit a homogeneous fine-grained microstructure (Ref 12). Wrought material, on the other hand, while being more expensive, offers advantages in terms of fewer internal defects, including lower chemical segregation and porosity (Ref 1, 2), and the certain development of a fine-grained microstructure during forging (Ref 11). Some researchers have also shown superior fatigue performance of wrought-forged components compared to cast-forged components for commercial Mg alloys (Ref 1, 13-16).

Previously, some research has compared the effect of the starting material state on the hot deformation behavior of

This invited article is part of a special topical focus in the *Journal of Materials Engineering and Performance* on Magnesium. The issue was organized by Prof. C. (Ravi) Ravindran, Dr. Raja Roy, Mr. Payam Emadi, and Mr. Bernoulli Andilab, Ryerson University.

Paresh Prakash, Jared Uramowski, and Mary A. Wells, Department of Mechanical and Mechatronics Engineering, University of Waterloo, 200 University Ave W, Waterloo, ON N2L 3G1, Canada; and **Bruce W. Williams**, CanmetMATERIALS, Natural Resources Canada, 183 Longwood Rd S, Hamilton, ON L8P 0A1, Canada. Contact e-mail: mawells@uwaterloo.ca.

various AZ alloys, but detailed characterization is mostly limited to the AZ31 alloy (Ref 7, 11, 17-20). Beer et al. have shown a higher tendency of the cast AZ31 alloy toward $\{10\bar{1}2\}$ tensile twinning compared to the extruded AZ31 alloy owing to its coarser initial grain size (Ref 19). Cast material also shows a slower DRX kinetics, leading it to show a bimodal microstructure at strains where the extruded material already shows a fine grained and homogenous microstructure (Ref 11), making the former a less suitable starting material for forging. Pilehva et al. have studied the effect of different starting microstructures on the hot compression behavior of the AZ91 alloy (Ref 7). Their results show that in the as-rolled state, dynamic recrystallization initiates at lower strains, lower temperatures, and the material shows a higher DRX% compared to the corresponding cast-homogenized material. A limitation of this study was that the compression tests were performed only up to a temperature of 300 °C and a strain of 0.5, whereas industrial forgings typically involve higher deformation strains, which can necessitate higher working temperatures for Mg alloys. Additionally, in all these studies, texture development during deformation was not investigated, while the texture is an important feature on which the material's deformation behavior and subsequent mechanical properties of the final component depends.

It is known that the microstructure and texture development during hot deformation in AZ alloys with a higher Al content (e.g. AZ80, AZ91, etc.) is very different compared to that in AZ31 (Ref 21-24). The present authors have recently shown that during hot compression at 400 °C, where Al is in solid solution in both AZ80 and AZ31 alloys, the DDRX grain size is larger in the AZ80, and it also shows a faster DDRX kinetics compared to the AZ31 alloy, such that by a strain of 1.0 a homogenized fine-grained microstructure develops in the former, while the latter shows a bimodal microstructure (Ref 25). These findings assume significance since a homogenized fine-grained microstructure is very desirable for the improved mechanical performance of the final component. The current research therefore investigates and compares the microstructure, texture, and flow stress evolution during uniaxial compression of as-cast and as-extruded AZ80 alloys at 400 °C, to gauge the suitability of using cast material as the starting material for forging. The research is part of a broader research project aiming to forge a full-scale automotive suspension component using the AZ80 magnesium alloy (Ref 14).

2. Experimental Details

The starting material was obtained in the form of direct-chill cast billets of about 300 mm diameter and extruded rods of 63.5 mm diameter from Magnesium Elektron North America Inc. Cylindrical samples measuring $\varnothing 10 \times 15$ mm were machined with their longitudinal axis parallel to the casting direction and extrusion direction, at a radial distance of 120 and 22 mm from the centerline of the cast billet and the extruded rod, respectively. The compositions of the cast billet and extruded rod as provided by the supplier are presented in Table 1.

Uniaxial compression tests were conducted using a Gleeble[®] 3500 thermal-mechanical simulator at a deformation temperature of 400 °C and constant true strain rates in the range of 0.001 to 0.1 s⁻¹. In a previous publication, the present authors have shown that at 400 °C the Mg₁₇Al₁₂ precipitates in the as-cast AZ80 alloy rapidly dissolve in the α -Mg matrix dur-

ing deformation, which thereby facilitates the interpretation of the results independent of the presence of the Mg₁₇Al₁₂ precipitates or the occurrence of PSN (Ref 26). The lateral surfaces of the samples were sprayed with a graphite-based lubricant prior to the compression tests to reduce friction during deformation. The samples were heated via electric resistive heating at a rate of 5 °C.s⁻¹ to the test temperature, soaked for 60 seconds, and then compressed at the desired strain rate. Thermocouple-based feedback from the deforming sample's surface was used to control the temperature during the tests. Samples were deformed to true strains of 0.05, 0.15, 0.4, and 1.0, and immediately quenched in water (within 1 second) to preserve the as-deformed microstructure.

Load–stroke data from the compression tests was converted to true stress–true strain data using the following equations,

$$\varepsilon = \ln\left(\frac{H_0 - \Delta H}{H_0}\right) \quad (\text{Eq 1})$$

$$\sigma = \frac{\text{Force}}{(\pi d_0^2 H_0 / 4 / (H_0 - \Delta H))} \quad (\text{Eq 2})$$

where ε is the calculated true strain value, σ is the calculated true stress value, H_0 is the initial height of the sample, ΔH is the change in height of the sample during deformation ($\Delta H = H_0 - H$, where H is the instantaneous height of the sample), and d_0 is the initial diameter of the sample. Uniaxially compressed samples become barrel-shaped during deformation due to friction, which is illustrated in the schematic shown in Fig. 1. In the schematic, H_0 and R_0 are the initial height and

Table 1 Composition of the alloys used in the present study (in wt.%)

	Al	Zn	Mn	Mg
Cast billet	8	0.31	0.15	balance
Extruded rod	8.2	0.33	0.14	balance

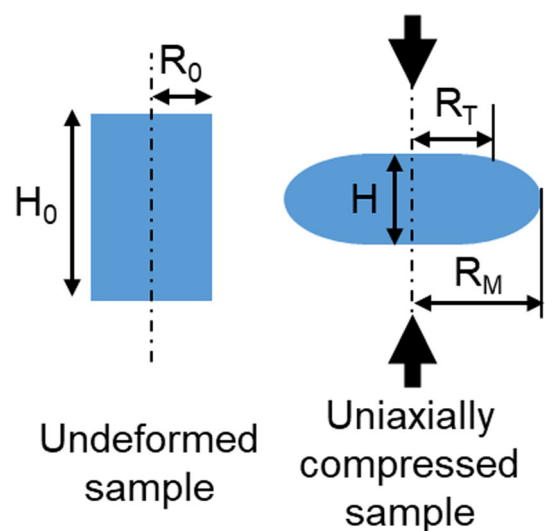


Fig. 1 Schematic showing barreling of cylindrical sample during hot compression due to friction

radius of the sample, while H is the instantaneous height during deformation and can be obtained from the stroke data of the Gleeble. R_T is the instantaneous top radius, while R_M is the instantaneous maximum radius (occurs at the sample mid-height level).

Flow stress data therefore must be corrected for friction, which is done in the present research following the method proposed by Ebrahimi in (Ref 27). Briefly, the diameters of the individual samples at the mid-height level (i.e., R_M) after compression to the strain of 1.0 were recorded. R_T was calculated using $R_T = \sqrt{\left(3\frac{H_0}{H}R_0^2 - 2R_M^2\right)}$, and was used to calculate $\Delta R = R_M - R_T$. R , or the instantaneous equivalent circular radius for the deforming sample if barreling had not occurred, can be calculated using $R = R_0\sqrt{H_0/H}$. Together these equations can be used to calculate the barreling shape parameter (b) and the friction factor (m) according to Eq 3 and 4, respectively. Note that H and R in Eq 3 and 4 correspond to the final height and final equivalent circular radius of the sample compressed to the strain of 1.0, and therefore give a single fixed value of m for specific starting material and deformation condition.

$$b = 4 \frac{\Delta R}{R} \frac{H}{\Delta H} \quad (\text{Eq 3})$$

$$m = \frac{(R/H)b}{(4/\sqrt{3}) - (2b/3\sqrt{3})} \quad (\text{Eq 4})$$

The experimental stress-strain curves were initially fit with a polynomial of order 6-10 degree to smoothen the curves, and subsequently the m values were used along with Eq 5 to calculate the friction corrected flow stress values (Ref 28).

$$\sigma_{corrected} = \frac{\sigma_{experimental}}{\left(1 + \frac{m}{3\sqrt{3}} \times \frac{R}{H}\right)} \quad (\text{Eq 5})$$

Detailed characterization of the microstructure and texture was performed only on the samples deformed at the strain rates of 0.001 and 0.1 s^{-1} . The deformed samples were sectioned longitudinally (about the compression axis), cold mounted in epoxy, and prepared according to the standard metallographic procedure for these alloys. The samples for electron backscatter diffraction (EBSD) were additionally chemically polished using a 10% Nital solution for up to 45 seconds. Samples for optical microscopy were etched using an acetic-picral solution.

EBSD was carried out using a FEI Nova NanoSEM-650 (FEG-SEM), equipped with an EDAX EDX detector, and operating at 20 kV. Step sizes of 0.75 and 0.5 μm were used for samples deformed at 0.001 and 0.1 s^{-1} , respectively, while the particular area that was scanned on each sample is as illustrated in Fig. 2. It is noted that the location of the dead metal zone and its extent in Fig. 2(a), (b) and (c) are simply a schematic (i.e., not to scale) and are included just for illustrative purposes. The true extent of the dead metal zone for one of the samples can be visualized in Fig. 2(d). Owing to a very coarse starting grain size of the as-cast material, a larger scan area compared to that for the extruded material needed to be scanned for the as-cast samples that were deformed to low strain levels, in order to acquire sufficient statistical data. The cast samples that were deformed to the strain of 1.0 were found to have a fine grained and homogeneous microstructure, which allowed for a much shorter EBSD scan area of 0.75 x 0.6 mm (which correspond to the scan area on all the extruded-deformed samples).

The scanned data were processed and analyzed using TSL OIM 8.0 software. Prior to the analysis, the data was cleaned using standard data cleaning techniques—initially an image quality-based thresholding was applied to remove the pixels affected by the presence of precipitates in the microstructure. Subsequently, one iteration of the neighbor orientation correlation (level 3), grain dilatation, and kernel average misorientation were performed (in that order) to correctly index the mis-indexed and un-indexed pixels. Additionally, the minimum grain size was set to 16 pixels, to avoid including spurious data involving a low number of pixels as real grains. High-angle boundaries (HABs) were defined as having misorientations of greater than equal to 10° .

X-ray diffraction (XRD) macrotexture measurements were performed using a Bruker D8-Discover diffractometer, equipped with a VÅNTEC-500 area detector, using Cu K_α radiation at 40 kV. A collimator of size 1 mm was used, and an area of about 1.5 x 2.5 mm was scanned on each sample. The diffraction data were processed using DIFFRAC.TEXTURE software, and the texture results are presented in terms of the (0002) basal pole figures.

3. Results and Discussion

3.1 Starting Material Characterization

The microstructure and texture of the starting materials are provided in Fig. 3 and 4, respectively. The as-cast material showed a coarse dendritic morphology, with a significant presence of $Mg_{17}Al_{12}$ precipitates, mainly at and around the grain boundaries. The extruded material showed a fine equiaxed grain morphology. The dark regions in the micrograph of the as-extruded material mark the $Mg_{17}Al_{12}$ precipitates in the lamellar morphology. Additionally, multiple Mn-Al based precipitates were also present in both the starting materials, albeit in very low amounts (totaling less than about 0.3 phase%). More detailed characterization of the precipitates is provided elsewhere (Ref 26). The $Mg_{17}Al_{12}$ phase dissolves rapidly in the α -Mg matrix during deformation at the test temperature of 400 $^\circ C$, while Mn-Al based precipitates are present only in low concentration, and therefore none of the precipitates are expected to play any significant role during hot deformation in the present research.

The grain size of the starting materials was determined using optical micrographs using the linear intercept method and multiplying it by a factor of 1.74 to account for the stereographic effects. The starting grain size was found to be $311.3 \pm 116.6 \mu m$ and $34.8 \pm 4.7 \mu m$ for the cast and extruded materials, respectively. The cast material showed a random texture, while the extruded material showed a preferential alignment of the basal poles perpendicular to the extrusion axis (Fig. 4), both textures being typical for mainstream Mg-alloys.

3.2 Microstructure Evolution and Dynamic Recrystallization

Micrographs of the cast and extruded deformed samples at 400 $^\circ C$ and 0.1 s^{-1} are presented in Fig. 5(a), (b), (c), (d) and (e), while Fig. 5(f) quantifies the low-angle boundary (LAB) fraction in the samples deformed to various strain levels. LABs have misorientations within 2- 10° and are quantified using the EBSD data. Figure 5(a), (b) and (c) shows optical micrographs. GB DRX and TDRX in Fig. 5(b) refer to grain boundary

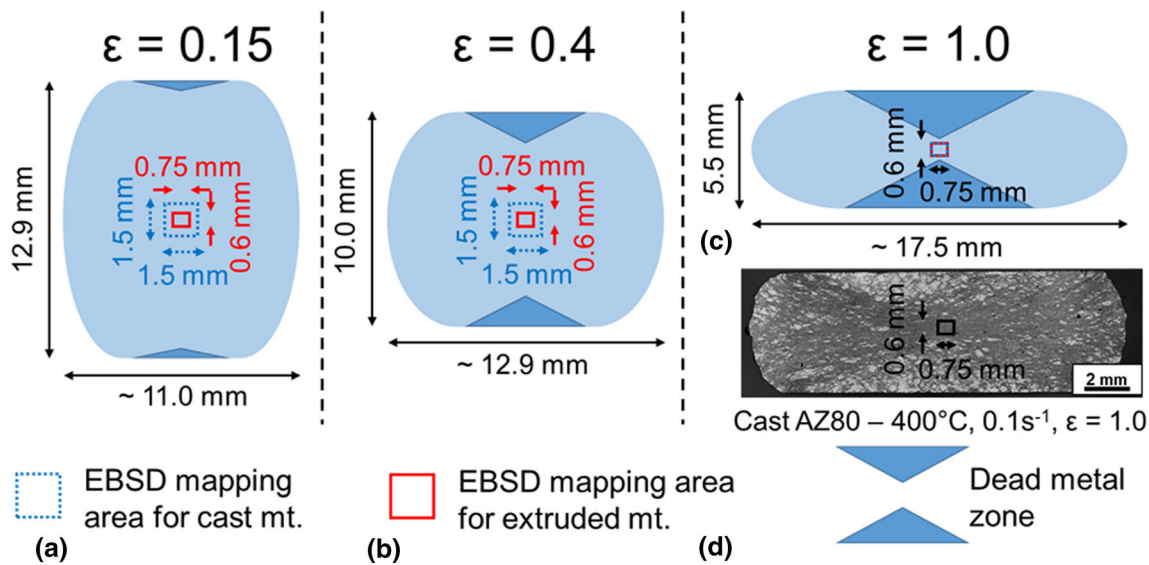


Fig. 2 Schematic showing the location and size of the EBSD scans on cast and extruded compressed samples during deformation. Sample size and the scan area are proportionally scaled. Image taken with permission from [29]

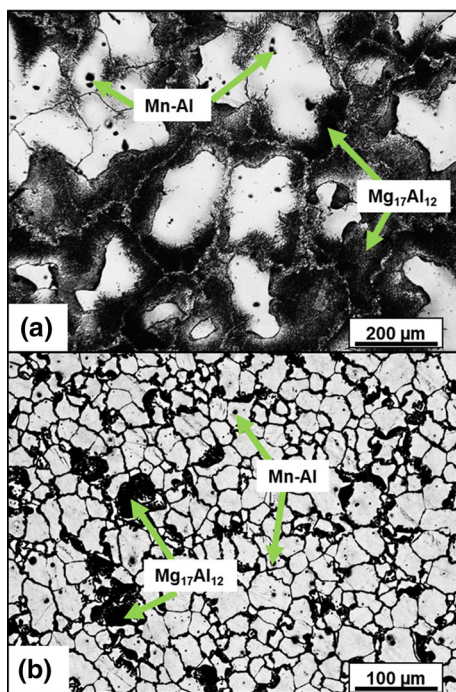


Fig. 3 Optical micrographs of as-received material (a) cast and (b) extruded AZ80 alloy. The major second phases in the alloys—Mg₁₇Al₁₂, and some Mn-Al-based precipitates—are marked in the micrographs

recrystallization and twin dynamic recrystallization, respectively. Figure 5(d) and (e) show EBSD inverse pole figure (IPF) maps colored with respect to the compression direction. LABs with 2-5 and 5-10° misorientations are marked as blue and red lines, respectively, while the high-angle boundaries, including the grain boundaries, are marked as black lines.

Considering the effect of hot deformation on the microstructure development in the cast material (Fig. 5a, b and c), an interesting feature to note is that the Mg₁₇Al₁₂ precipitates dissolved rapidly during the deformation such that in the

sample deformed to the strain of 0.15 there is no visual evidence of any of these precipitates remaining. The as-cast samples that were deformed at 0.1 s⁻¹ showed the occurrence of {10 $\bar{1}$ 2}<10 $\bar{1}$ 1> tensile twinning at low strain levels (Fig. 5a), while these twins were found to recrystallize at higher deformation strains (an example of this is shown in Fig. 5b). The twin type was identified based on the characteristic peak at 86° in the misorientation angle distribution plot developed using the EBSD data. Recrystallization within the twins is not investigated any further in the present research, but prior literature on comparable alloys indicate that this can take place through multiple mechanisms, including: 1) intersection of twins leading to the formation of twin-walled grains, which then grow, and 2) formation of low-angle boundaries (LABs) bounded substructure within the twins, which eventually convert to separate grains by absorption of dislocations by the LABs during continued deformation. These mechanisms can be subsumed under the common heading *twin dynamic recrystallization* (TDRX) (Ref 5, 8, 30). The sample compressed to the strain of 0.4 (not shown in the figure) did not show any twins, suggesting that twinning was exhausted at lower strains, and either the twins were fully recrystallized (through TDRX), or the entire grains in which the twins nucleated twinned completely during the deformation.

Discontinuous dynamic recrystallization (DDRX) at prior grain boundaries through grain boundary serration and bulging was identified as another major DRX mechanism. The micrograph in Fig. 5(c) shows clear evidence of serrated grain boundaries in the cast sample deformed at 400 °C and 0.1 s⁻¹. Due to deformation and slip, grain boundaries become serrated, and at some favorable locations these serrated portions can bulge into the neighboring grain by the movement of the grain boundary, which is driven by the dislocation density gradient across the grain boundary. Subsequently this bulged region can rotate due to deformation, resulting in the formation of a low-angle boundary (LAB) which separates the bulged region from the parent grain (Ref 31). Eventually, this low-angle boundary absorbs dislocations during continued deformation and transforms to a high-angle boundary, thus separating the bulged

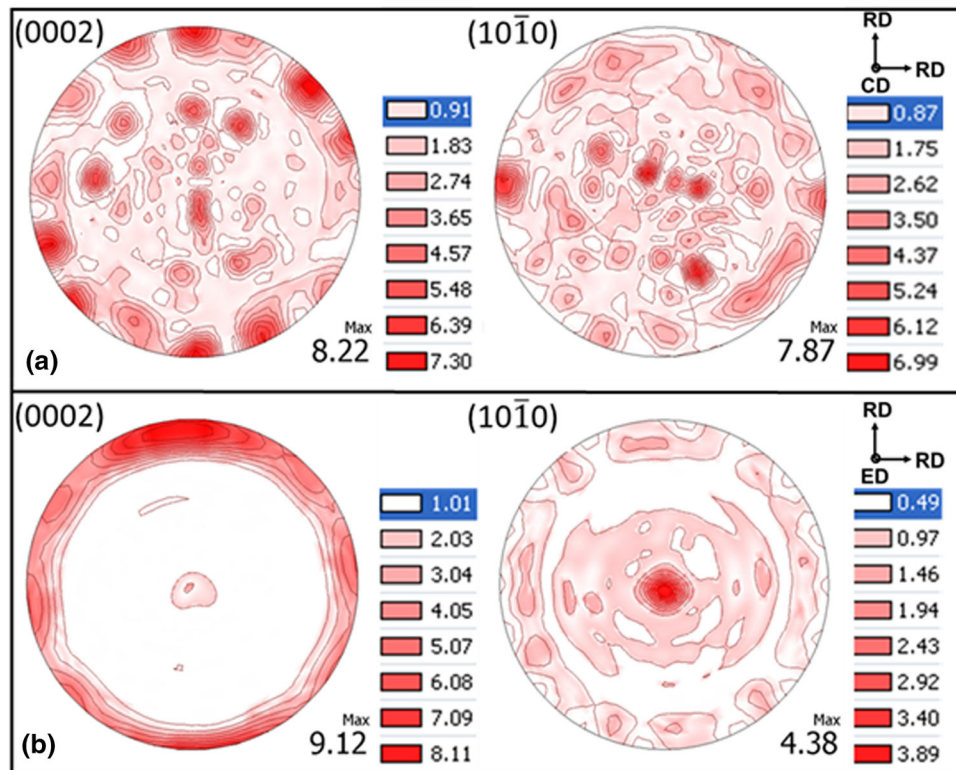


Fig. 4 XRD macrottextures of as-received (a) cast and (b) extruded samples. Orientation legend—CD: casting direction, ED: extrusion direction, RD: radial direction

region from the parent grain (Ref 10). A bulged region and the LAB separating it from the parent grain can be seen in the EBSD IPF map of cast deformed sample presented in Fig. 5(d). DDRX is supposed to have initiated in the material somewhere in the strain range of 0.05 to 0.15, as was inferred based on no visual evidence of DDRXed grains in the sample deformed to the strain of 0.05, while a noticeable presence of such grains in the sample deformed to the strain of 0.15.

Deformation also resulted in the fragmentation of the original grains by the development and criss-crossing of kink bands (some kink bands are marked in Fig. 5d). This resulted in the formation of LABs bounded substructures, which eventually converted into separate grains through dislocation absorption during continued deformation. This indicates that continuous dynamic recrystallization (CDRX) also contributed to the grain refinement and microstructure development. Previously, we have shown that relative trends in the LAB fraction can be used as an indicator of the relative occurrence of CDRX during deformation of cast AZ31 and AZ80 alloys (Ref 25), and a similar kind of analysis is extended here for the present results. Figure 5(f) compares the LAB fraction ($2\text{-}10^\circ$) in the cast and extruded deformed samples at 400°C . The cast deformed samples showed relatively higher LAB fractions compared to the corresponding extruded deformed samples at low strain levels suggesting that the cast material showed a slightly higher tendency for CDRX compared to the extruded material. Note that in the samples deformed to the strain of 0.15 at 400°C and 0.1 s^{-1} , the extruded material showed an unusually high LAB fraction, and it is not known currently what could have caused this. At higher strains at both the strain rates, the LAB fraction in the two starting materials became comparable, which can be related to their microstructure

becoming comparable due to deformation and DRX (refer to Fig. 6, 7 and 8a).

Microstructure evolution in the extruded material at 400°C and 0.1 s^{-1} (Fig. 5e) was comparable to that in the cast alloy, including the occurrence of DDRX and CDRX, except for the occurrence of twinning and TDRX. Twinning is expected to not have taken place in the extruded material owing to its relatively fine grain size (Ref 32). The cast and extruded samples that were deformed at 0.001 s^{-1} showed comparable microstructural features as in Fig. 5(a), (b), (c), (d) and (e), except for the occurrence of twinning even in the cast samples. Twinning is not expected to have taken place at the lower strain rate since the applied rate of deformation was low enough to be adequately accommodated by slip-based deformation modes. Typically, a single dominant DRX mechanism depending on the deformation conditions and texture is reported for Mg alloys in hot deformation studies (Ref 10, 33, 34), but in the present research both DDRX and CDRX were found to be significant contributors to the DRX. Previously, Beer et al. have also reported a simultaneous and significant occurrence of DDRX and CDRX during hot compression of cast and extruded AZ31 alloys for a range of deformation conditions (Ref 11).

Microstructure evolution with deformation strain for the two starting materials is presented through the EBSD IPF maps in Fig. 6 and 7, for deformation at 0.1 and 0.001 s^{-1} , respectively. The micrographs show that in both the starting materials DDRX initially took place at the prior grain boundaries, resulting in the formation of a *necklace microstructure* at low strain levels. With progressive deformation, the area covered by the DDRXed grains increased, such that by a strain of 1, a homogenous fine-grained microstructure had developed in both the cast and extruded deformed samples. It is interesting to see

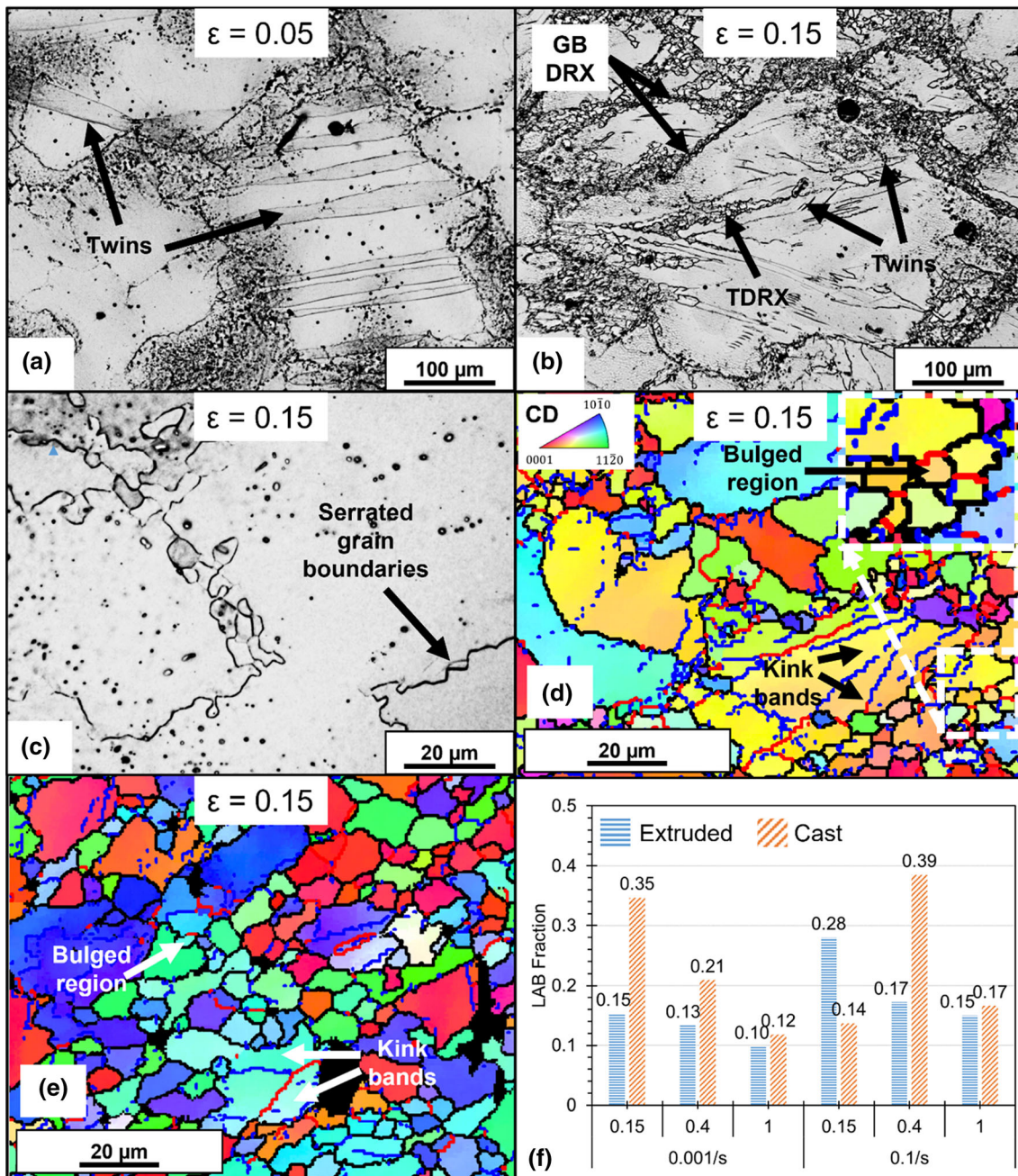


Fig. 5 Microstructure features of interest during deformation of the cast and extruded AZ80 samples: (a-d) are of cast deformed samples, while (e) is of extruded deformed sample. Inset in (d) shows higher magnification image of the region bounded by the white box in the main micrograph. (f) Low-angle boundary (LAB) fraction variation in the deformed samples

the development of a comparable microstructure in the two starting materials despite having very different initial microstructures and grain sizes. This is attributed to a higher tendency of the cast material for CDRX compared to the extruded material (Fig. 5f), as well as a faster DDRX kinetics in the later stages of deformation in the case of the former (results presented later). Both the overall grain sizes and the DDRX grain sizes were comparable in the two starting materials after deformation to the strain of 1 (Fig. 8a and b). It is noteworthy that the microstructure of the extruded material deformed at 0.001 s^{-1} (lower row in Fig. 7) does not seem to have changed much with deformation strain, owing to a similarity of the

DDRX grain size with that of the extruded material's initial grain size.

The EBSD data are used to quantify the microstructure and the results are presented in Fig. 8. The substructure and eventual grains formed by CDRX vary significantly in size in the same microstructure itself (as can be gauged from Fig. 5d and e), and because of this it is impractical to quantify the CDRX grain size and % in the microstructure. However, the overall grain size can be quantified, as well as the DDRX grain size and DDRX%. DDRX grains are characterized by low misorientation gradients within the newly formed grains and can be identified using a grain orientation spread (GOS)-based criteria, which can directly be defined in the EBSD data

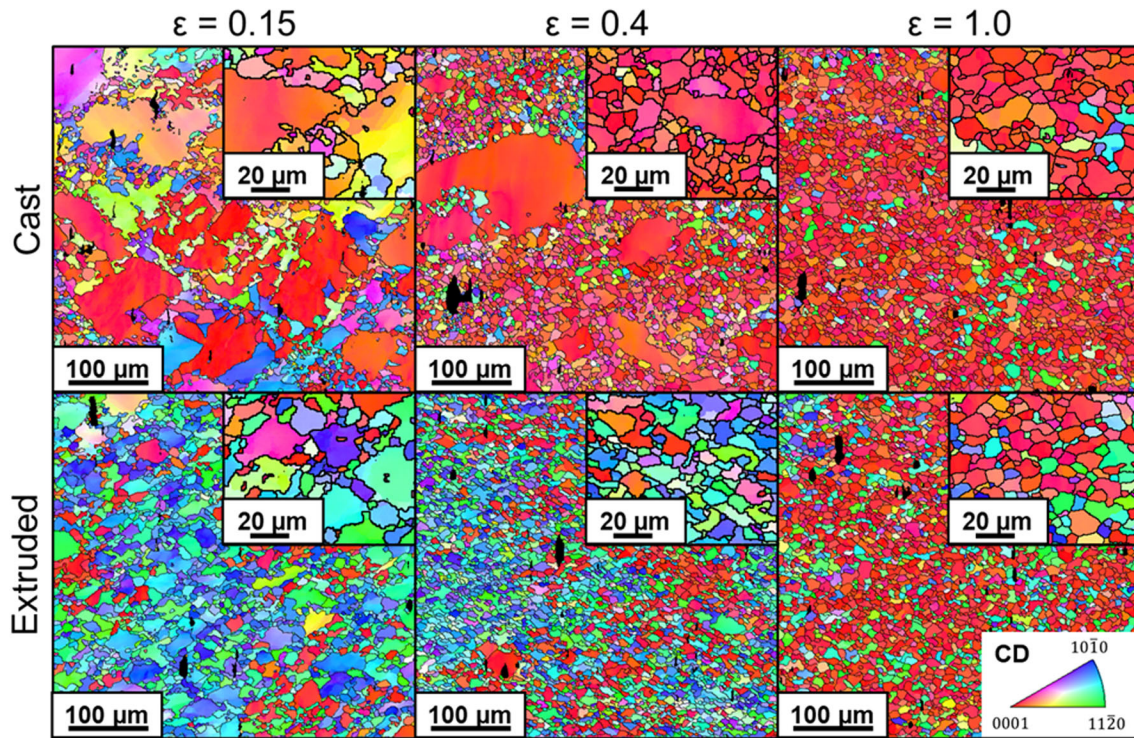


Fig. 6 EBSD IPF maps of cast and extruded samples deformed at 400 °C and 0.1 s⁻¹, showing microstructure evolution with deformation strain. Inset images represent high magnification micrographs

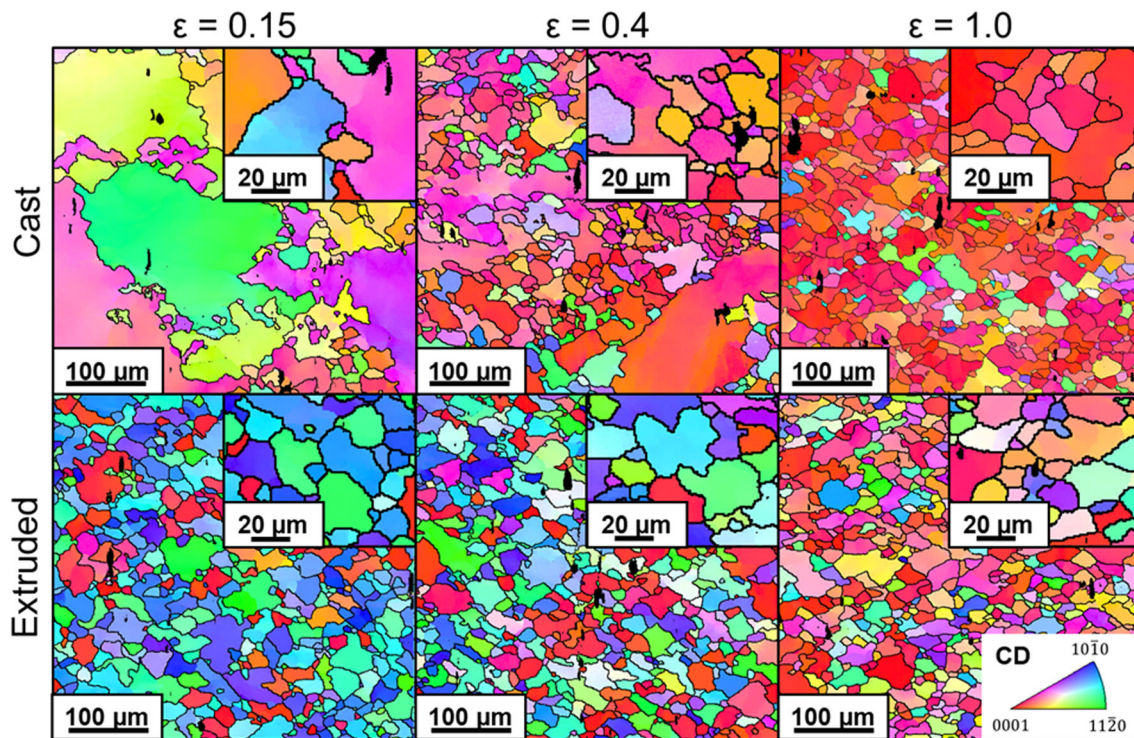


Fig. 7 EBSD IPF maps of cast and extruded samples deformed at 400 °C and 0.001 s⁻¹, showing microstructure evolution with deformation strain

analysis software (Ref 35). Typically, a GOS value of up to 2° is used for DDRXed grains, while higher GOS values are used for deformed grains (Ref 35). Previously, we have shown that a GOS ≤ 2° is suitable to identify DDRXed grains in the cast

AZ80 alloy deformed at 400 °C (Ref 25). However, since the as-extruded starting material is expected to have been significantly recrystallized during its prior extrusion processing, using a GOS of ≤ 2° results in the inclusion of many less

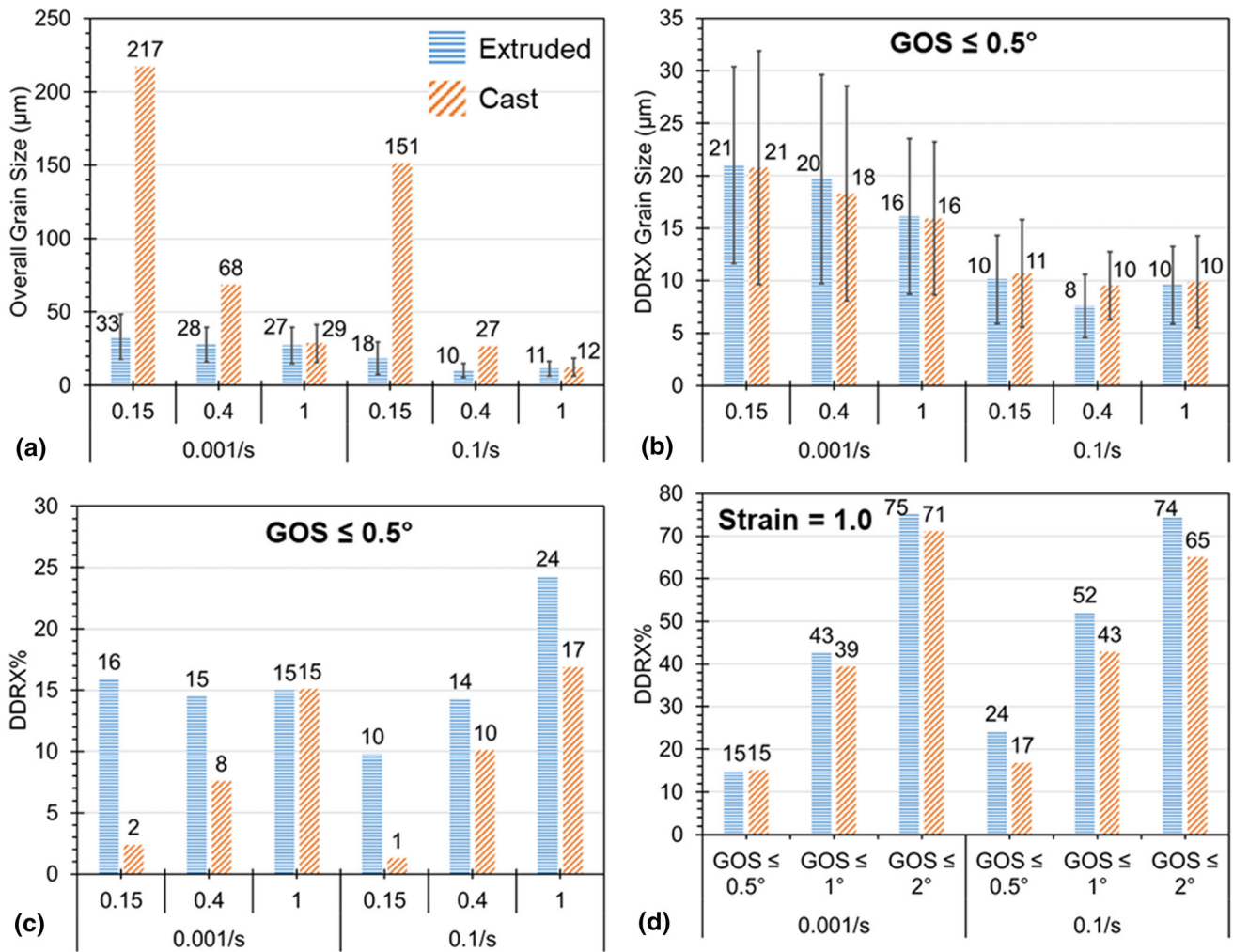


Fig. 8 Microstructure quantification results based on the EBSD data: (a) Overall grain size, (b) DDRX grain size, (c) DDRX%, and (d) DDRX%'s dependence on GOS value used for partitioning, for samples deformed to the strain of 1. Horizontal axis in (a-c) represents deformation strain level at the two strain rates, while in (d) represents different GOS values

deformed grains as DDRXed grains, especially in the samples deformed to a relatively low strain of 0.15, and this could introduce a bias to the analysis. To make a fair quantitative comparison with the cast deformed samples, a GOS of $\leq 0.5^\circ$ instead was found more suitable and was used in the present research.

Figure 8(a) shows that despite significantly different initial grain sizes, the cast and extruded samples showed comparable grain size values after deformation to a strain of 1. Figure 8 (b) shows that the DDRX grain size was independent of the deformation strain level and was similar for the cast and extruded starting materials. The invariance of the DDRX grain size on the deformation strain level is well established (Ref 11, 36, 37), and while it is generally accepted that the DDRX grain size is independent of the grain size of the starting material (Ref 38, 39), some authors have reported a finer DDRX grain size in the case of a finer grained starting material (Ref 40).

Figure 8(c) shows the evolution of DDRX% in the two starting materials during deformation, where the extruded deformed samples showed a much higher DDRX% compared to the corresponding cast deformed samples, especially at low strain levels. An interesting observation is that the DDRX% remained relatively stable at around 15% in the extruded

samples deformed at the strain rate of 0.001 s^{-1} , suggesting that the microstructure was always in equilibrium with deformation. The higher DDRX% in the extruded material compared to the cast material can be explained considering the much smaller initial grain size in the case of the former, which provides a higher specific grain boundary area for DDRX nucleation (Ref 11, 39). The DDRX% reported in Fig. 8(c) is low, which is attributed to the use of a very low GOS value ($\text{GOS} \leq 0.5^\circ$) in its plotting, since using such low values of GOS essentially limits the analysis to only the most recently recrystallized grains. Using higher GOS values capture more grains as DDRXed grains, resulting in a higher DDRX%, as is illustrated in Fig. 8(d). However, this can also lead to the inclusion of recrystallized-deformed grains in the DDRX grains' dataset which can affect the analysis.

3.3 Texture Evolution

The textures of the deformed samples are presented in Fig. 9. As stated previously, the as-cast material had a random texture, while the as-extruded material had a preferential distribution of the basal poles perpendicular to the prior extrusion axis (Fig. 4). The texture of the as-extruded material

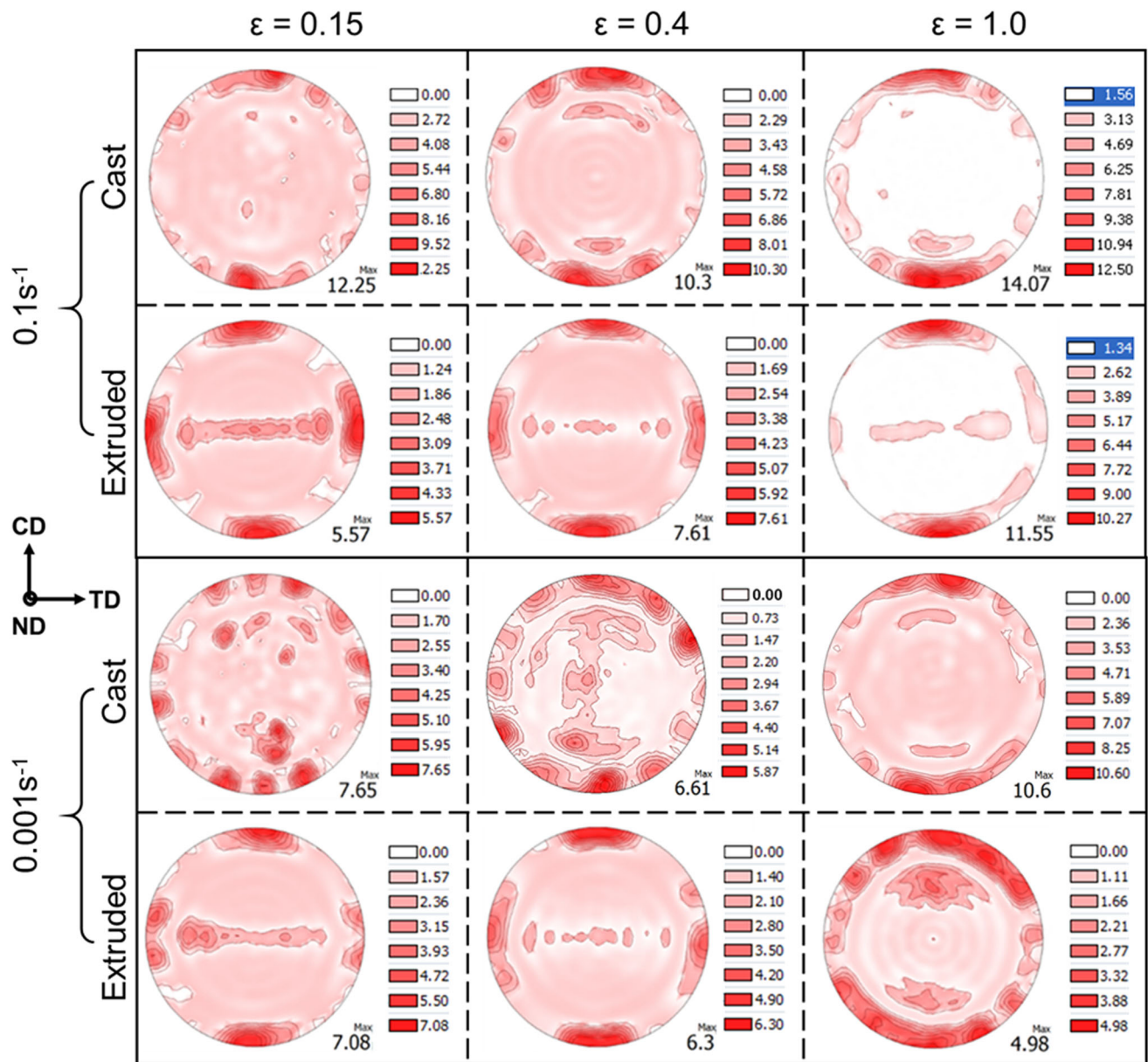


Fig 9 XRD macrotextures of cast and extruded samples deformed at 400 °C. Orientation legend—CD: compression direction, ND: normal direction, and TD: transverse direction

about the compression direction (CD) can be visualized more clearly in Fig. 10(a), which also shows the partitioning of the starting texture of the as-extruded material into three components about the CD to facilitate the interpretation of the results (partitioning done using the EBSD data). The components A, B, and C divide the grains in the starting extruded material into three partitions based on the orientation of their c-axis with respect to the CD - A : 0-20°, B : 20-70°, and C : 70-90° to the CD.

Considering the texture evolution in the cast-deformed samples at 0.1 s⁻¹ (Fig. 9), the basal poles rapidly rotated toward the CD during deformation to the strain of 0.15, which is attributed to a substantial occurrence of {10 $\bar{1}$ 2}<10 $\bar{1}$ 1> tensile twinning in the cast material during deformation. Once this sharp basal texture developed, the texture remained relatively stable during any further deformation. Considering the texture development in the extruded-deformed samples at

0.1 s⁻¹, the grains initially oriented along the component C gradually rotated into the component B, and eventually into the component A, as the deformation progressed, resulting in the development of a near basal texture along the CD. A gradual texture change is indicative of slip-based deformation, while an absence of sudden texture reorientations (as in the case of the corresponding cast-deformed samples) indicates that twinning did not take place in the extruded samples. At 0.001 s⁻¹, the cast material also showed a gradual rotation of the basal poles toward the CD as the deformation progressed, indicating slip-based deformation and an absence of twinning (Ref 41). The texture results therefore support the microstructure-based findings described earlier that twinning only took place in the cast material, and only at the higher strain rate.

The extruded samples that were deformed at the lower strain rate (0.001 s⁻¹) showed a gradual weakening of the texture, suggesting texture randomization. Texture randomization can

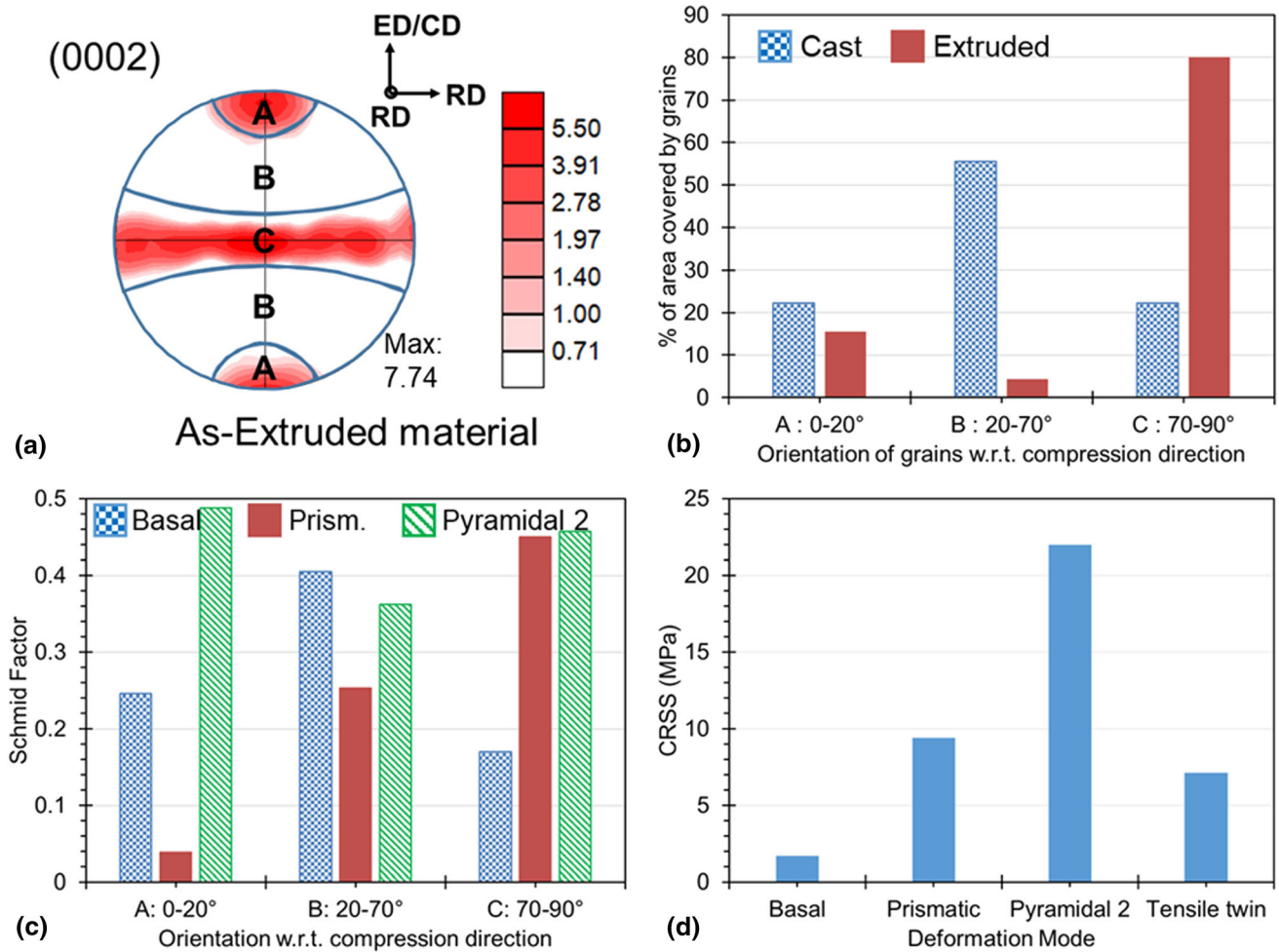


Fig. 10 (a) (0002) basal pole figure of the as-extruded material showing partitioning of the starting texture into components A, B, and C about the compression direction (CD), (b) % of grains (area wise) oriented within specific orientation range w.r.t. the CD, (c) Schmid factor (SF) for the major slip modes for grains oriented along components A, B, and C, and (d) CRSS for the major deformation modes in pure Mg at 400 °C

take place due to DRX, as has been reported earlier for the extruded AZ31 alloy (Ref 42). To investigate whether this is the case for the extruded AZ80 alloy in the present research, the textures of the DDRXed grains and non-DDRXed regions were plotted separately using the EBSD data and compared (Fig. 11). A GOS of $\leq 0.5^\circ$ was used for the DDRXed grains, to reduce the possibility of including DDRXed-deformed grains in this dataset. The pole figures presented in Fig. 11 suggest that the DDRXed grains followed the orientations of the parent grains (i.e., the non-DDRXed regions), indicating that texture randomization did not take place.

It is interesting to analyze what could have caused the observed texture weakening in the extruded samples deformed at 0.001 s^{-1} if it was not caused by DDRX. Further discussion in this regard is facilitated by considering the graphs plotted in Fig. 10. Note that Fig. 10(a), (b) and (c) are plotted using the EBSD data, while the data for (d) was taken from literature on pure Mg for deformation at 400 °C (Ref 4). Figure 10(a) partitions the grains in the starting extruded material into three components, according to the orientation of their c-axis with respect to the compression direction, as described previously. Figure 10(b) plots the area fractions of the grains oriented along these components for the cast and extruded starting materials. Figure 10(c) plots the component-wise average Schmid factor

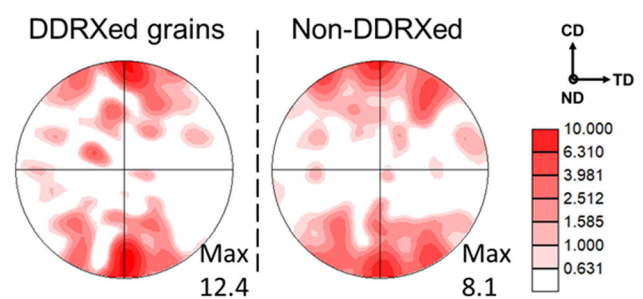


Fig. 11 Partitioned (0002) basal pole figures of the DDRXed grains and the non-DDRXed regions in the extruded sample deformed at 400 °C and 0.001 s^{-1} to a strain of 1

(SF) values, while Fig. 10(d) plots the critical resolved shear stress (CRSS) of the dominant deformation modes in pure Mg at 400 °C. Note that the plot for the cast material in Fig. 10(b) assumes a perfect random texture.

Figure 10(b) shows that the vast majority of the grains ($\sim 80\%$) in the starting extruded material were oriented along the component C. Figure 10(c) shows that for such grains the prismatic slip ($\{10\bar{1}0\}\langle 11\bar{2}0\rangle$) and the second-order pyramidal slip ($\{11\bar{2}2\}\langle 11\bar{2}\bar{3}\rangle$), hereafter referred to as the pyramidal 2

slip, have the highest SF values, while Fig. 10(d) shows that the CRSS for the prismatic slip is much lower compared to that of the pyramidal 2 slip at 400 °C. These results, when considered together, suggest that most of the grains in the extruded material deformed via the prismatic slip, which is known to cause grain rotation only about the c-axis (Ref 41), and therefore is not expected to result in the rotation of the grains toward the CD. At the same time, it is expected that the basal slip ($(0002) \langle 11\bar{2}0 \rangle$), owing to a very low CRSS (Fig. 10d), and the pyramidal 2 slip, owing to a high SF (Fig. 10c), were active to a limited extent in the grains originally oriented along the component C. Prevalence of multiple slip system activity delayed the rotation of these grains toward a common orientation (i.e., toward a sharp texture) (Ref 43), which is observed here for the extruded samples deformed at 0.001 s^{-1} as an apparent weakening of the texture with deformation strain. It is suggested that the texture of the sample deformed to the strain of 1.0 (lower most row in Fig. 9) was still in transition, whereby grains initially oriented along the component C were somewhere mid-way through their reorientation toward the CD (as a result of basal slip and pyramidal 2 slip (Ref 41), which resulted in the development of a weak overall texture in the material. For deformation at 0.1 s^{-1} , the extruded material did show the preservation of the C component with deformation strain to a certain extent (refer to the corresponding pole figures in Fig. 9) due to prismatic slip activity; however, the increased strain rate is suggested to have shifted the dominant deformation mode to basal and pyramidal 2 slips, which resulted in the development of a near basal texture in the material.

Considering texture development in the cast deformed samples, a majority of the grains in the starting as-cast material were oriented along the component B (Fig. 10b), which together with the data plotted in Fig. 10(c) and (d) suggest that the cast material deformed majorly by the (0002) basal slip, which results in basal texture development along the CD (Ref 41). At 0.001 s^{-1} , this indeed seems to have taken place considering the macrotexture results presented in Fig. 9. At 0.1 s^{-1} , twinning also took place to complement the basal slip as an additional deformation mode, owing to a low CRSS value, and a relatively favorable orientation of the grains (oriented along the components B and C) about the CD, and significantly accelerated the basal texture development in these samples.

3.4 Flow Stress Curves

The flow stress curves of the cast and extruded samples deformed at 400 °C at different strain rates are presented in Fig. 12(a). A typical flow curve shows rapid strain hardening to a peak in the flow stress, followed by a gradual softening to a steady state flow stress at higher strain levels. The peak and subsequent flow stress softening occur when the dislocation annihilation rate due to DDRX exceeds the strain hardening rate caused by dislocation generation and entanglement because of deformation. The steady state occurs once an equilibrium is established between strain hardening and DDRX and recovery related softening effect. At lower strain rates, the extruded material showed lower peak stresses, while at higher strain rate it showed higher peak stress, when compared to the corresponding cast deformed samples. Previously, Beer et al. have shown similar results for AZ31 alloy, whereby extruded material is shown to have lower peak stress compared to the cast material at lower Z conditions, while the trends reversed

under high Z conditions (Ref 19). Note that Z is the Zener–Hollomon parameter ($Z = \dot{\epsilon} * \exp(\frac{Q}{RT})$), where $\dot{\epsilon}$ is the strain rate, Q is the deformation activation energy, R is the universal gas constant, and T is the deformation temperature in Kelvin). Referring to Fig. 12(a), the flow stress gradually reduced following the peak, due to the occurrence and progress of DDRX, and eventually a common steady state flow stress was achieved in the two starting materials, owing to the development of comparable microstructures and textures.

The precise strain at which DDRX initiates in the material can be obtained based on a mathematical analysis of the flow stress curve proposed by Poliak and Jonas (Ref 44), but is typically approximated as a constant fraction of the peak strain (the strain corresponding to the peak in the flow stress curve) (Ref 45, 46). The peak strain in the samples deformed at 0.01 and 0.1 s^{-1} are plotted in Fig. 12 (b), and lower values of the peak strain in case of the extruded material indicate that the DDRX initiated in it at lower strains.

Figure 12(c) plots the strain hardening rate (θ) as a function of deformation strain from peak strain onwards for the two starting materials at the strain rates of 0.01 and 0.1 s^{-1} . The strain hardening rate following the peak strain can be assumed to indicate DDRX kinetics in the material, with lower θ values (i.e., more negative values) indicating faster DDRX kinetics (Ref 47). The extruded material showed much lower θ values immediately following the peak compared to the cast material, suggesting a much faster DDRX kinetics. Beyond slightly higher strains, the cast material started showing lower θ values, suggesting it started showing faster DDRX kinetics compared to the extruded material. The $\theta_{Ex} \ll \theta_{Cast}$ and $\theta_{Ex} > \theta_{Cast}$ regions are labeled in Fig. 12(c) for samples deformed at 0.1 s^{-1} for easy reference. Though not investigated in the present research, the peculiar material behavior might be related to the initial grain boundaries of the as-extruded material quickly becoming saturated with the DDRX grains due to a fast DDRX kinetics close to the peak strain. A consequence of faster DDRX kinetics at later stages of deformation in the cast material (along with a relatively higher tendency for CDRX—refer to Fig. 5(f) and accompanying discussion), is that it catches up with the extruded material in terms of the microstructure development by a strain of 1.

It is interesting to note that the interpretation of the strain hardening rate plot in Fig. 12(c) in terms of DDRX kinetics at the minimum θ values (which occur approximately in the strain range of 0.1 to 0.2 for different samples) nicely compliments the DDRX nucleation rate data (Fig. 12d) at the deformation strain of 0.15. The DDRX nucleation rate is approximated based on the number of the DDRXed grains per unit EBSD scan area in the microstructure, with the DDRX grains identified using a GOS of $\leq 0.5^\circ$ to limit the data to only the recently DDRXed grains. The extruded sample deformed at the higher strain rate showed a higher DDRX nucleation rate compared to the sample deformed at the lower strain rate and correspond well with the lower minimum θ value shown by the former in Fig. 12(c). With regard to the cast material, the DDRX nucleation rates at the two strain rates were comparable at the deformation strain of 0.15 and correspond well with the comparable minimum θ values shown by the cast material at the two strain rates in Fig. 12(c). Also, a much higher DDRX nucleation rate in case of the extruded material compared to the cast material is also captured well by the corresponding minimum θ values in Fig. 12(c). At higher strains this

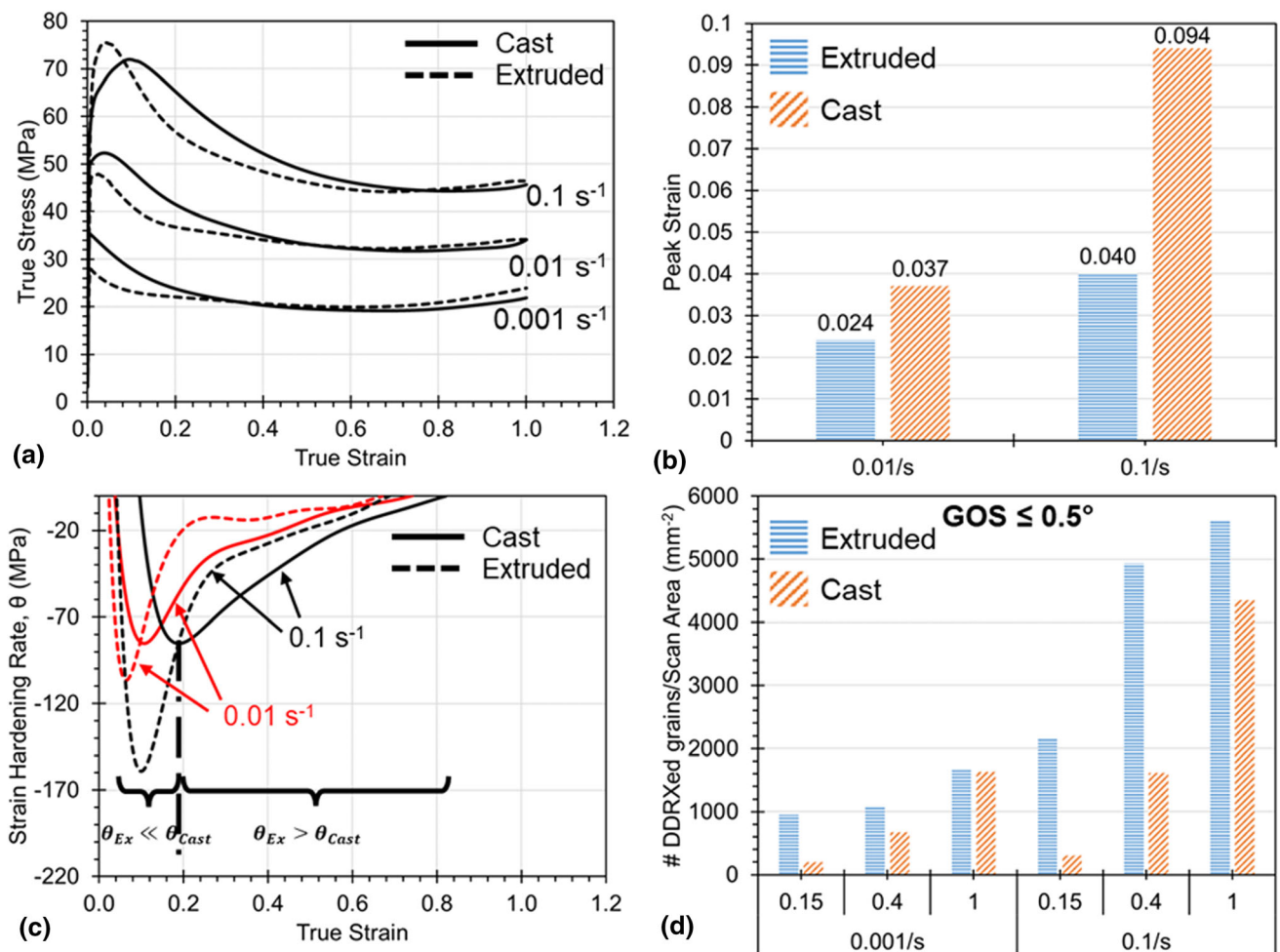


Fig. 12 (a) Measured flow stress curves, (b) peak strain at 0.01 and 0.1 s⁻¹, and (c) strain hardening rate plots for samples deformed at 0.01 and 0.1 s⁻¹, and (d) Number of DDRXed grains per unit scan area as an indicator of the DDRX nucleation rate. Horizontal axis in (d) represents strain level at the two strain rates.

correspondence between the DDRX nucleation rate and the θ values seem to have been lost, presumably because the softening of the flow curve is additionally dependent on factors other than the DDRX kinetics, such as texture, as well.

4. Conclusions

Microstructure, texture, and flow stress evolution of the cast and extruded AZ80 alloy during uniaxial hot compression was studied at 400 °C and strain rates ranging from 0.001 to 0.1 s⁻¹. Both materials show occurrence of dynamic recrystallization, mainly through the discontinuous dynamic recrystallization (DDRX) and continuous dynamic recrystallization (CDRX) mechanisms, resulting in a substantial grain refinement from the initial state. The DDRX grain size is found to be independent of the nature of the starting material, including the initial grain size. In the later stages of deformation, a relatively faster DDRX kinetics, along with a relatively higher tendency for CDRX, allows the microstructure development of the cast material to approach that of the extruded material. By a strain of 1, a homogeneous fine-grained microstructure with similar grain sizes develop in both the starting materials.

Simultaneously, a comparable basal deformation texture develops in all the samples, although this development is slightly slower in the extruded material, owing to most of the grains in the starting material deforming through the prismatic slip. The two starting materials show a common steady state flow stress value, which is attributed to the development of comparable microstructures and textures due to deformation.

Industrial forgings typically experience strains much higher than 1, which together with the above conclusions suggests that cast material, including cast pre-form shapes, may indeed be used as the starting material for forging applications, in-lieu of wrought material. To ensure industrial suitability, more research may be necessary to compare the mechanical properties of components forged from cast and wrought materials. Further, if forging is to be conducted at lower temperatures, the effects of Mg₁₇Al₁₂ precipitates on the deformation behavior of these materials must also be considered.

Acknowledgment

The authors would like to gratefully acknowledge the financial support of the Natural Sciences and Engineering Research Council of Canada (NSERC), Automotive Partnership Canada (APC)

program under APCPJ 459269—13 Grant with contributions from Multimatic Technical Centre, Ford Motor Company, and Centerline Windsor. The authors would like to thank Mr. Mark Whitney and Dr. Massimo Di Ciano of UW for help in carrying uniaxial compression tests; Prof. Hamid Jahed and Dr. Sugrib Shaha of UW for help in acquiring XRD texture data; and Ms. Renata Zavadil of CanmetMATERIALS for help in EBSD data acquisition.

Data Availability

The raw/processed data required to reproduce these findings cannot be shared at this time as the data also forms part of an ongoing study. Specific data will be made available on request.

References

- Z.B. Sajuri, Y. Miyashita, Y. Hosokai, and Y. Mutoh, Effects of Mn Content and Texture on Fatigue Properties of As-Cast and Extruded AZ61 Magnesium Alloys, *Int. J. Mech. Sci.*, 2006, **48**(2), p 198–209
- S.M.H. Karparvarfard, S.K. Shaha, S.B. Behraves, H. Jahed , and B.W. Williams, Fatigue Characteristics and Modeling of Cast and Cast-Forged ZK60 Magnesium Alloy, *Int. J. Fatigue*, 2019, **118**, p 282–297
- J. Hirsch and T. Al-Samman, Superior Light Metals by Texture Engineering: Optimized Aluminum and Magnesium Alloys for Automotive Applications, *Acta Materialia*, 2013, **61**(3), p 818–843
- A. Chapuis and J.H. Driver, Temperature Dependency of Slip and Twinning in Plane Strain Compressed Magnesium Single Crystals, *Acta Materialia*, 2011, **59**(5), p 1986–1994
- T. Al-Samman and G. Gottstein, Dynamic Recrystallization During High Temperature Deformation of Magnesium, *Mater. Sci. Eng. A*, 2008, **490**(1–2), p 411–420
- P. Changizian, A. Zarei-Hanzaki , and H. Abedi, On the Recrystallization Behavior of Homogenized AZ81 Magnesium Alloy: The Effect of Mechanical Twins and γ Precipitates, *Mater. Sci. Eng. A*, 2012, **558**, p 44–51
- F. Pilehva, A. Zarei-Hanzaki , and S.M. Fatemi-Varzaneh, The Influence of Initial Microstructure and Temperature on the Deformation Behavior of AZ91 Magnesium Alloy, *Mater. Design*, 2012, **42**, p 411–417
- S.W. Xu, S. Kamado, N. Matsumoto, T. Honma , and Y. Kojima, Recrystallization Mechanism of As-Cast AZ91 Magnesium Alloy During Hot Compressive Deformation, *Mater. Sci. Eng. A*, 2009, **527**(1–2), p 52–60
- X. Yang, H. Miura , and T. Sakai, Dynamic Evolution of New Grains in Magnesium Alloy AZ31 during Hot Deformation, *Mater. Trans.*, 2003, **44**(1), p 197–203
- A. Galiyev, R. Kaibyshev , and G. Gottstein, Correlation of Plastic Deformation and Dynamic Recrystallization in Magnesium Alloy ZK60, *Acta Materialia*, 2001, **49**(7), p 1199–1207
- A.G. Beer and M.R. Barnett, Microstructural Development during Hot Working of Mg–3Al–1Zn, *Metal. Mater. Trans. A*, 2007, **38**, p 1856–1867
- T. Kodippili, S. Lambert , and A. Arami, Data-Driven Prediction of Forging Outcome: Effect of Preform Shape on Plastic Strain in a Magnesium Alloy Forging, *Mater. Today Commun.*, 2022, **31**, p 103210
- A. Gryguc, S.B. Behraves, S.K. Shaha, H. Jahed, M. Wells, B. Williams , and X. Su, Low-Cycle Fatigue Characterization and Texture Induced Ratcheting Behaviour of Forged AZ80 Mg Alloys, *Int. J. Fatigue*, 2018, **116**, p 429–438
- A. Gryguć, S. Behraves, H. Jahed, M. Wells, B. Williams, R. Gruber, A. Duquette, T. Sparrow, J. Prsa , and X. Su, A Method for Comparing the Fatigue Performance of Forged AZ80 Magnesium, *Metals*, 2021, **11**(8), p 1–16
- D. Toscano, S. K. Shaha, B. Behraves, H. Jahed, M. Wells, B. Williams , and J. McKinley, “Effect of Forging on Microstructure, Texture and Compression Behavior of Extruded AZ31B,” *Proceedings of the 3rd Pan American Materials Congress*, pp. 347–354, 2017
- D. Toscano, S.K. Shaha, B. Behraves, H. Jahed , and B. Williams, Effect of Forging on Microstructure, Texture, and Uniaxial Properties of Cast AZ31B Alloy, *J. Mater. Eng. Performance*, 2017, **26**, p 3090–3103
- M. Graf, M. Ullmann , and R. Kawalla, Influence of Initial State on Forgeability and Microstructure Development of Magnesium Alloys, *Procedia Eng.*, 2014, **81**, p 546–551
- Y. Liu, J. Zhou, D. Zhang, T. Lin, Y. Liu, C. Tian , and Y. Yang, Influence of Initial Microstructure on the Hot Working Flow Stress of Mg–3Al–1Zn Alloy, *Materials Science Forum*, 2017, **898**, p 86–90
- A. Beer and M. Barnett, Influence of Initial Microstructure on the Hot Working Flow Stress of Mg–3Al–1Zn, *Mater. Sci. Eng. A*, 2006, **423**(1–2), p 292–299
- B. Wang, R. Xin, G. Huang, X. Chen , and Q. Liu, Hot-Deformation Behaviors of AZ31 Alloys with Different Initial States, *Trans. Nonferrous Metals Soc. China*, 2008, **18**(1), p s145–s149
- X. Huang, K. Suzuki, Y. Chino , and M. Mabuchi, Influence of Aluminum Content on the Texture and Sheet Formability of AM Series Magnesium Alloys, *Mater. Sci. Eng. A*, 2015, **633**, p 144–153
- F. Guo, D. Zhang, H. Wu, L. Jiang , and F. Pan, The Role of Al Content on Deformation Behavior and Related Texture Evolution During Hot Rolling of Mg–Al–Zn Alloys, *J. Alloys Compounds*, 2017, **695**, p 396–403
- Q. Wang, Y. Chen, M. Liu, J. Lin , and H.J. Roven, Microstructure Evolution of AZ Series Magnesium Alloys During Cyclic Extrusion Compression, *Mater. Sci. Eng. A*, 2010, **527**(9), p 2265–2273
- F. Zarendi, G. Seale, R. Verma, E. Essadiqi , and S. Yue, Effect of Al and Mn Additions on Rolling and Deformation Behavior of AZ Series Magnesium Alloys, *Mater. Sci. Eng. A*, 2008, **496**(1–2), p 159–168
- P. Prakash, M.A. Wells , and B.W. Williams, Hot Deformation of Cast AZ31 and AZ80 Magnesium Alloys – Influence of Al Content on Microstructure and Texture Development, *J. Alloys Compounds*, 2022, **897**, p 162876
- P. Prakash, D. Toscano, S.K. Shaha, M.A. Wells, H. Jahed , and B.W. Williams, Effect of Temperature on the Hot Deformation Behavior of AZ80 Magnesium Alloy, *Mater. Sci. Eng. A*, 2020, **794**, p 139923
- R. Ebrahimi and A. Najafizadeh, A New Method for Evaluation of Friction in Bulk Metal Forming, *J. Mater. Process. Technol.*, 2004, **152**(2), p 136–143
- R. Hill, *The Mathematical Theory of Plasticity*, Oxford University Press, 1998
- P. Prakash, *Microstructure and texture evolution during hot deformation of AZ80 magnesium alloy*, University of Waterloo, Waterloo, 2019
- O. Sitdikov, R. Kaibyshev , and T. Sakai, “Dynamic Recrystallization Based on Twinning in Coarse-Grained Mg,” 2003
- A.M. Wusatowska-Sarnek, H. Miura , and T. Sakai, Nucleation and Microtexture Development Under Dynamic Recrystallization of Copper, *Mater. Sci. Eng. A*, 2002, **323**(1–2), p 177–186
- M.R. Barnett, Z. Kehsavaz, A.G. Beer , and D. Atwell, Influence of Grain Size on the Compressive Deformation of Wrought Mg–3Al–1Zn, *Acta Materialia*, 2004, **52**(17), p 5093–5103
- D. Qin, M. Wang, C. Sun, Z. Su, L. Qian , and Z. Sun, Interaction Between Texture Evolution and Dynamic Recrystallization of Extruded AZ80 Magnesium Alloy during Hot Deformation, *Mater. Sci. Eng. A*, 2020, **788**, p 139537
- Y. Huang, G. Zeng, L. Huang, Z. Zheng, C. Liu , and H. Zhan, Influence of Strain Rate on Dynamic Recrystallization Behavior and Hot Formability of Basal-Textured AZ80 Magnesium Alloy, *Mater. Character.*, 2022, **187**, p 111880
- A. Hadadzadeh, F. Mokdad, M.A. Wells , and D.L. Chen, A New Grain Orientation Spread Approach to Analyze the Dynamic Recrystallization Behavior of a Cast-Homogenized Mg–Zn–Zr Alloy, *Mater. Sci. Eng. A*, 2018, **709**, p 285–289
- J.P. Sah, G.J. Richardson and C.M. Sellars, Grain-Size Effects during Dynamic Recrystallization of Nickel, *Metal Sci.*, 1974, **8**(1), p 325–331
- S.M. Fatemi-Varzaneh, A. Zarei-Hanzaki , and H. Beladi, Dynamic Recrystallization in AZ31 Magnesium Alloy, *Mater. Sci. Eng. A*, 2007, **456**(1–2), p 52–57
- C.M. Sellars, Recrystallization of Metals, *Metals Forum*, 1981, **4**, p 75–80
- M.R. Barnett, A.G. Beer, D. Atwell , and A. Oudin, Influence of Grain Size on Hot Working Stresses and Microstructures in Mg–3Al–1Zn, *Scripta Materialia*, 2004, **51**(1), p 19–24

40. H. Watanabe, H. Tsutsui, T. Mukai, K. Ishikawa, Y. Okanda, M. Kohzu , and K. Higashi, Grain Size Control of Commercial Wrought Mg-Al-Zn Alloys Utilizing Dynamic Recrystallization, *Mater. Trans.*, 2001, **42**(7), p 1200–1205
41. S.R. Agnew, M.H. Yoo , and C.N. Tomé, Application of Texture Simulation to Understanding Mechanical Behavior of Mg and Solid Solution Alloys Containing Li or Y, *Acta Materialia*, 2001, **49**(20), p 4277–4289
42. P. Backx and L. Kestens, Dynamic Recrystallization during Compression of Mg-3%Al-1%Zn, *Mater. Sci. Forum*, 2005, **495–497**, p 633–638
43. T. Al-Samman, X. Li , and S.G. Chowdhury, Orientation Dependent Slip and Twinning During Compression and Tension of Strongly Textured Magnesium AZ31 alloy, *Mater. Sci. Eng. A*, 2010, **527**(15), p 3450–3463
44. E.I. Poliak , and J.J. Jonas, A One-Parameter Approach to Determining the Critical Conditions for the Initiation of Dynamic Recrystallization, *Acta Materialia*, 1996, **44**(1), p 127–136
45. J. Wang, J. Chen, Z. Zhao , and X.-Y. Ruan, Dynamic Recrystallization Behavior of Microalloyed Forged Steel, *J. Iron and Steel Res. Int.*, 2008, **15**(3), p 78–81
46. M.R. Barnett, Hot Working Microstructure Map for Magnesium AZ31, *Mater. Sci. Forum*, 2003, **426–432**, p 515–520
47. J.J. Jonas, X. Queleñec, L. Jiang , and É. Martin, The Avrami Kinetics of Dynamic Recrystallization, *Acta Materialia*, 2009, **57**(9), p 2748–2756

Publisher's Note Springer Nature remains neutral with regard to jurisdictional claims in published maps and institutional affiliations.

Springer Nature or its licensor holds exclusive rights to this article under a publishing agreement with the author(s) or other rightsholder(s); author self-archiving of the accepted manuscript version of this article is solely governed by the terms of such publishing agreement and applicable law.